

Superstructures of oxygen and sulphur on a Fe(110) surface via fast atom diffraction

A. Schüller, M. Busch,* J. Seifert, S. Wethekam, and H. Winter

Institut für Physik, Humboldt Universität zu Berlin, Newtonstrasse 15, D-12489 Berlin-Adlershof, Germany

K. Gärtner

Institut für Festkörperphysik, Friedrich-Schiller-Universität Jena, Max-Wien-Platz 1, D-07743 Jena, Germany

(Received 19 February 2009; revised manuscript received 14 May 2009; published 19 June 2009)

Fast helium atoms and hydrogen molecules with energies from 400 eV up to several keV are grazing scattered from a Fe(110) surface covered by oxygen and sulphur atoms forming $c(2 \times 2)$ and $c(1 \times 3)$ superstructures, respectively. For scattering along low-index azimuthal directions we observe defined diffraction patterns in the angular distributions for scattered projectiles. From the evaluation of those diffraction patterns we derive the widths of low-indexed axial channels, the corrugation of the interaction potential across these channels, and the normal positions of adsorbed atoms above the Fe lattice. Our analysis is based on semiclassical models using hard-wall approximation as well as individual potentials for the interaction of projectiles with the surface. By comparing the results of different models, we discuss the robustness of the information on the geometrical structure of the surfaces.

DOI: [10.1103/PhysRevB.79.235425](https://doi.org/10.1103/PhysRevB.79.235425)

PACS number(s): 79.20.Rf, 79.60.Bm, 34.20.Cf, 68.49.Bc

I. INTRODUCTION

Diffraction and interference effects for scattering of particles with finite-rest mass can be understood in the framework of quantum physics using the concept of matter waves by de Broglie¹. Diffraction phenomena were first observed for scattering of low-energy electrons from a metal surface² and of thermal He atoms from an alkali-halide surface³. Both findings were milestones for establishing quantum mechanics. For electrons with energies of typically 100 eV or He atoms with energies of about 50 meV the de Broglie wavelength is of the same order of magnitude as the interatomic spacings in crystals. Hence, scattering of low-energy electron diffraction and reflection high-energy electron diffraction [LEED (Refs. 4 and 5) and RHEED,⁶ respectively] as well as scattering of thermal atoms (thermal energy atom scattering-TEAS and helium atom scattering-HAS)⁷⁻⁹ have been developed to powerful tools for structural investigations of crystalline surfaces. However, electron scattering is inadequate for surface structures which are affected by electron-stimulated desorption¹⁰, dissociation¹¹, reconstruction¹², or rearrangement.¹³ Furthermore, it is predominantly applicable to conducting surfaces. On the other hand, scattering of thermal atoms can be affected by the adsorption of atoms or molecules from the residual gas and as e.g., the formation of hydrogen superstructures due to the long recording times caused by inefficient detection.

The recently introduced method of fast atom diffraction (FAD) is nondestructive, has a high detection efficiency, is sensitive to the topmost layer only, and can be applied to insulator surfaces at room or elevated temperatures. Therefore, this method is suitable for investigations of sensible surface structures where established techniques might fail. In the meantime, FAD has been demonstrated for grazing scattering of light atoms and molecules with projectile energies of about 1 keV from monocrystalline insulator¹⁴⁻¹⁷ and metal^{18,19} surfaces as well as metal surfaces covered with adsorbate superstructures²⁰ at room temperature.

For scattering under grazing angles of incidence^{21,22}, fast atoms, ions, molecules, or molecular ions are steered by

strings (“axial channeling”) or planes (“planar channeling”) of lattice atoms. Under such conditions, projectile trajectories can be separated in two widely decoupled regimes of scattering: (1) a “fast” one for the motion parallel to the atomic strings or planes with energy $E_{\parallel} = E_0 \cos^2 \Phi_{\text{in}} \approx E_0$, where E_0 is the initial projectile energy and Φ_{in} is the polar-incidence angle with respect to the surface plane, and (2) a “slow” motion normal with respect to strings or planes of surface atoms with energy $E_{\perp} = E_0 \sin^2 \Phi_{\text{in}} \ll E_0$ (for, e.g., $\Phi_{\text{in}} = 1$ deg holds $E_{\perp} = 3 \times 10^{-4} E_0$). The de Broglie wavelengths $\lambda_{\text{dB}} = h/Mv = h/\sqrt{2ME_0}$ (h = Planck constant, M = projectile mass, and v = projectile velocity) associated to the parallel and normal motion are given by $\lambda_{\text{dB}\parallel} = h/\sqrt{2ME_{\parallel}} = \lambda_{\text{dB}}/\cos \Phi_{\text{in}} \approx \lambda_{\text{dB}}$ and $\lambda_{\text{dB}\perp} = h/\sqrt{2ME_{\perp}} = \lambda_{\text{dB}}/\sin \Phi_{\text{in}} \gg \lambda_{\text{dB}}$, respectively. While $\lambda_{\text{dB}\parallel}$ is 2 to 3 orders of magnitude smaller compared to interatomic spacings of surfaces, $\lambda_{\text{dB}\perp}$ is comparable to lattice spacings for light atoms and molecules with projectile energies up to some keV. The positions of diffraction spots are determined by the Bragg condition for constructive interference in the surface plane: $n\lambda_{\text{dB}} = d \sin \Psi / \cos \Phi_{\text{out}} \approx d \sin \Psi$,¹⁷ with d being the distance between adjacent strings of surface atoms, n the diffraction order, Ψ the azimuthal exit angle within the surface plane, and Φ_{out} the polar exit angle (cf. Fig. 1). The Bragg condition for Ψ corresponds to a relation for constructive interference in the detection plane, which is perpendicular to the axial strings of surface atoms: $n\lambda_{\text{dB}\perp} = d \sin \Theta$ with $\Theta \approx \arcsin(\sin \Psi / \sin \Phi_{\text{in}})$ being the deflection angle. The Bragg condition $n\lambda_{\text{dB}} = d \sin \Psi$ implies that the positions of diffraction spots in the detection plane depend on the de Broglie wavelength λ_{dB} (i.e., on the velocity v or projectile energy E_0) only, but are independent of the polar-incidence angle Φ_{in} . On the other hand, owing to the Bragg condition $n\lambda_{\text{dB}\perp} = n\lambda_{\text{dB}}/\sin \Phi_{\text{in}} = d \sin \Theta$, diffraction spots appear under the same deflection angle Θ for different λ_{dB} , if Φ_{in} is adjusted in order to achieve same $\lambda_{\text{dB}\perp}$. The diffraction conditions for the normal motion can be interpreted in terms of an enlarged de Broglie wavelength $\lambda_{\text{dB}\perp}$, which is for graz-

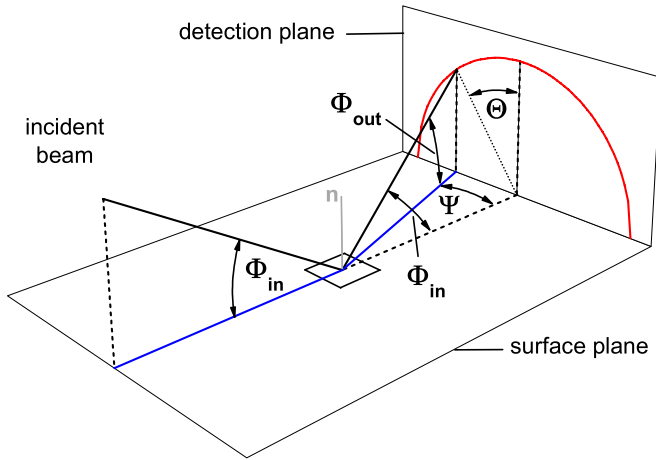


FIG. 1. (Color online) Sketch of scattering geometry.

ing scattering about a factor of 100 larger than λ_{dB} and of the same order of magnitude as the interatomic spacings in the crystal lattice.

In recent works^{19,20} we have shown that from the evaluation of diffraction patterns for low-indexed axial channels one can deduce their widths and the corrugation of the interaction potential across these channels. Furthermore, for the scattering from superstructures on a substrate surface, one can estimate the transverse position of adsorbate atoms from the corrugation of the potential. This paper describes recent progress on this topic. We present a detailed evaluation of diffraction patterns for the scattering of He atoms and H₂ molecules from a $c(1 \times 3)$ superstructure of sulphur and a $c(2 \times 2)$ superstructure of oxygen on a Fe(110) surface. The corrugation for the $c(2 \times 2)$ O/Fe(110) superstructure is determined in the framework of the *hard-wall* approximation taking into account a correction with respect to deviations caused by the softness of a more realistic potential.

In Fig. 2, we display a sketch of structural models for the two superstructures, which have been investigated experimentally^{23–35} and theoretically^{36–42} before. For both superstructures, the adsorbate atoms occupy fourfold hollow sites of the Fe substrate. The $c(1 \times 3)$ S/Fe(110) structure is formed at a sulphur coverage of $\theta=1/3$ ML and the $c(2 \times 2)$ O/Fe(110) structure at an oxygen coverage of $\theta=1/4$ ML. The normal height h of the adsorbate above the topmost Fe layer was calculated with density functional theory (DFT): 1.39 Å for $c(1 \times 3)$ S/Fe(110) (Ref. 38) and 1.0 Å for the $c(2 \times 2)$ O/Fe(110) superstructure³⁹. The value for the $c(2 \times 2)$ O/Fe(110) superstructure will be compared with the analysis of our data obtained via FAD.

The paper is organized as follows. In Sec. II we describe our experimental setup and the preparation of superstructures on the Fe(110) crystal. In Sec. III A we present the results of the LEED measurements. The determination of the angular positions of the FAD spots is given in Sec. III B. In Sec. III C we evaluate the intensity modulation of the FAD spots and demonstrate the generation of diffraction charts. In Sec. III D we discuss the soft-potential correction for the hard wall approximation. In Sec. III E we demonstrate the determination of the vertical positions of adsorbed oxygen atoms. Conclusions are given in Sec. IV.

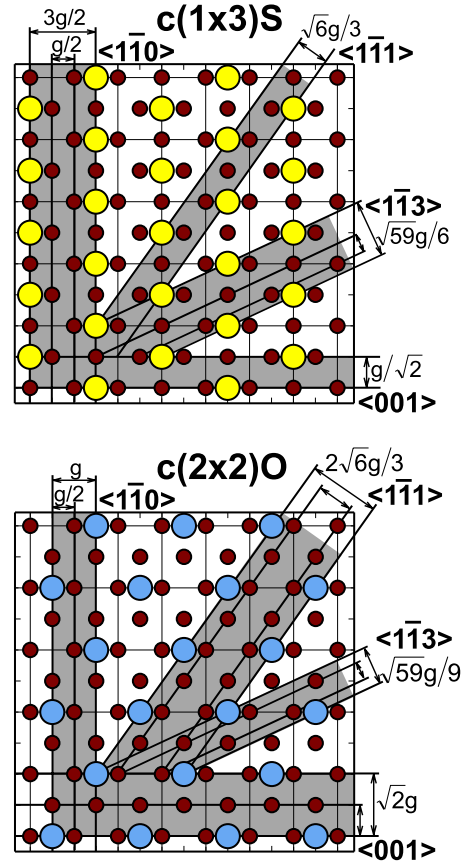


FIG. 2. (Color online) Sketch of top view of structural models for $c(1 \times 3)$ S/Fe(110) (upper panel) and $c(2 \times 2)$ O/Fe(110) (lower panel). Some low indexed axial channels are highlighted. Widths d of channels are given with respect to Fe lattice constant $g = 2.86$ Å (Ref. 23) (see also Table I). Fe atoms of first (110) layer: small dark red circles, S atoms (upper panel): large yellow circles and O atoms (lower panel): large blue circles.

II. EXPERIMENT

In our experiments, we have scattered neutral H₂ molecules, ³He and ⁴He atoms with projectile energies E_0 ranging from 0.4 keV up to several keV from an adsorbate covered Fe(110) surface at room temperature under grazing angles of incidence $\Phi_{in} \leq 1.5$ deg. Fast-ion beams (energy width $\leq 2\%$) were produced in a 10 GHz electron-cyclotron resonance (ECR) ion source (Nanogan-Pantechneque, Caen, France). The neutralization of the He⁺ and H₂⁺ ions was achieved via charge transfer in a gas cell mounted in the beam line of the accelerator operating with He or Kr gas, respectively. Residual ions were removed by electric field plates. The atomic beams are collimated by sets of vertical and horizontal slits of 0.2 mm widths to a beam divergence smaller than 0.03 deg (adjustable). These slits are parts of differential pumping stages in order to maintain a base pressure of mid 10^{-11} mbar in our UHV chamber. The Fe(110) target surface was prepared by cycles of grazing sputtering with 25 keV Ar⁺ ions and subsequent annealing to about 770 K for 15 min. The cleanness and flatness of the surface was checked by Auger electron spectroscopy (CLAM2, VG Scienta) and low-energy electron diffraction (SPALEED, Omi-

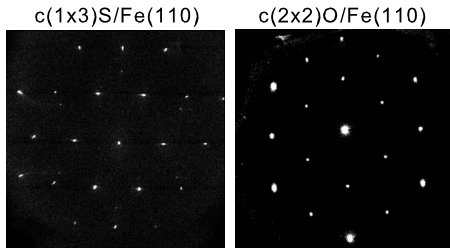


FIG. 3. LEED patterns of superstructures $c(1 \times 3)S/Fe(110)$ (left panel) and $c(2 \times 2)O/Fe(110)$ (right panel) for electron energies of 120 eV (left panel) and 91 eV (right panel).

ron Nanotechnology GmbH). Superstructures with sulphur atoms were produced in several cycles of annealing at 1000 K by segregation from bulk impurities of the crystal,^{24–26} and superstructures with oxygen atoms by adsorption of O_2 for a dose of 2 L (1 L=1 Langmuir= 1.33×10^{-6} mbar s) at a pressure of 5×10^{-9} mbar at room temperature and subsequent annealing at 770 K for 10 min.³⁵ Using SPALEED,

we observed sharp spots for the superstructures $c(1 \times 3)S/Fe(110)$ and $c(2 \times 2)O/Fe(110)$. Two-dimensional angular distributions of scattered projectiles were recorded at a distance of 0.66 m behind the target with a position sensitive microchannel plate (MCP) detector (Roentdek GmbH⁴³) with a spatial resolution of $\delta\Psi=0.01^\circ$. This provides a simple and efficient procedure for recording data, where complete diffraction patterns, as shown below, can be recorded in a time of some minutes with a count rate of about 10^3 per second for an incident particle flux of the same order of magnitude. This is a substantial advantage compared to thermal energy helium atom scattering where the detection of atoms is less efficient by orders of magnitude and time consuming.

III. RESULTS AND DISCUSSION

A. LEED measurements

Figure 3 shows LEED patterns of the superstructures $c(1 \times 3)S$ and $c(2 \times 2)O$ on Fe(110), which are recorded at

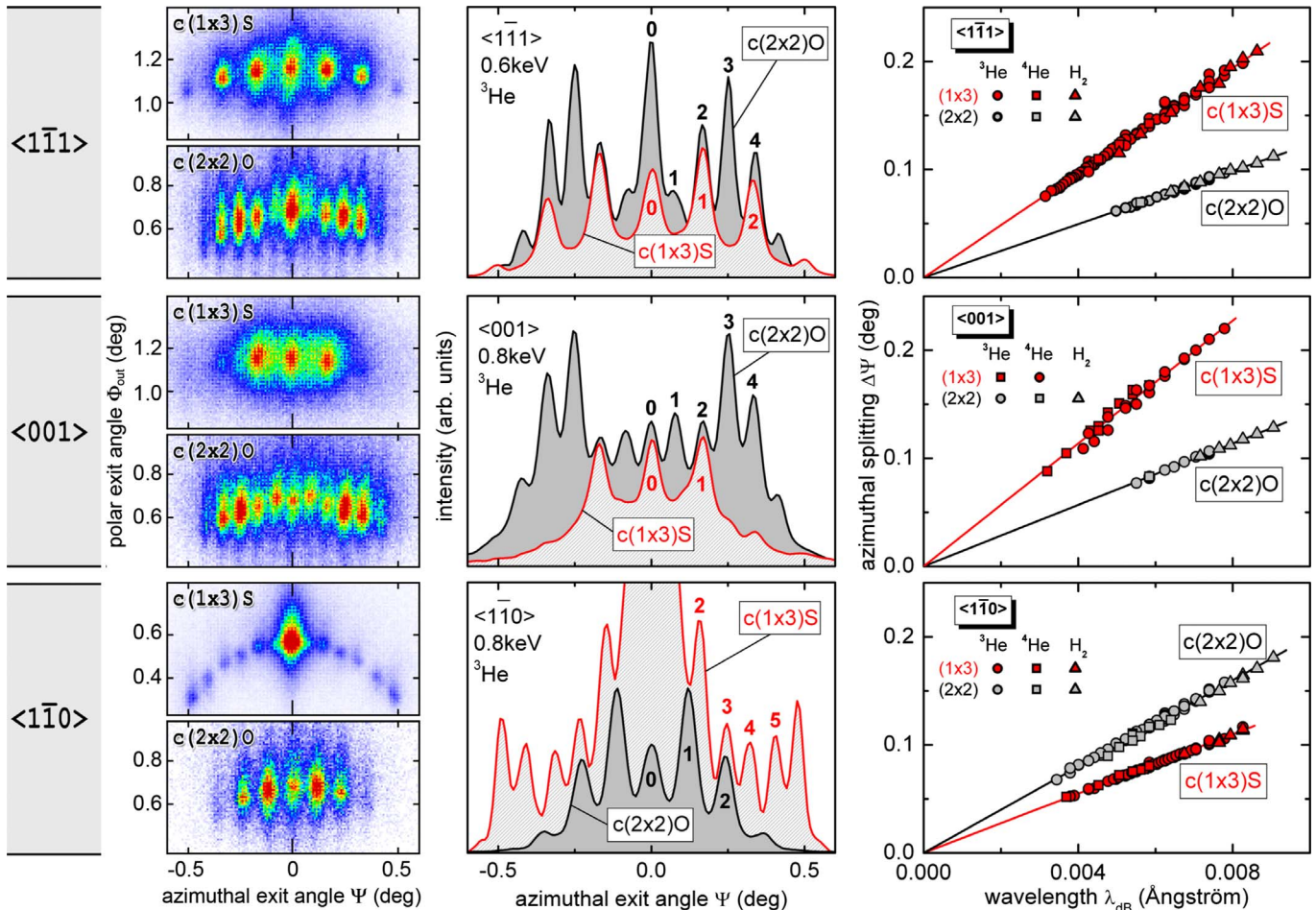


FIG. 4. (Color online) Two-dimensional intensity distributions as recorded with microchannel plate detector (left column) and projections on azimuthal exit angle Ψ (middle column) for scattering of 0.6 keV (upper row) and 0.8 keV (middle and lower row) 3He atoms along $\langle 1\bar{1}1 \rangle$ (upper row), $\langle 001 \rangle$ (middle row), and $\langle 1\bar{1}0 \rangle$ (lower row) directions from $c(1 \times 3)S/Fe(110)$ (red curves in middle column) and from $c(2 \times 2)O/Fe(110)$ (black curves in middle column) under $0.6 \text{ deg} \leq \Phi_{in} \leq 1.2 \text{ deg}$. Color code for two-dimensional intensity distributions: red=high intensity, blue=low intensity. Right column: Azimuthal angular splittings $\Delta\Psi$ of diffraction spots as function of λ_{dB} for scattering of H_2 molecules, 3He and 4He atoms from $c(1 \times 3)S/Fe(110)$ (red symbols) and $c(2 \times 2)O/Fe(110)$ (gray symbols) along $\langle 1\bar{1}1 \rangle$ (upper row), $\langle 001 \rangle$ (middle row), and $\langle 1\bar{1}0 \rangle$ (lower row) directions. Red and gray lines: best linear fits to data.

electron energies of 120 eV and 91 eV, respectively. The centered-rectangular lattice of Fe(110) can be identified in the LEED pattern of the $c(2 \times 2)\text{O}/\text{Fe}(110)$ superstructure (right panel of Fig. 3), where the substrate spots are somewhat more pronounced in comparison to the superstructure spots. The LEED pattern of the $c(2 \times 2)\text{O}/\text{Fe}(110)$ superstructure is similar to the observations in Refs. 28 and 34. The $c(1 \times 3)\text{S}$ LEED pattern is similar to the patterns shown in Refs. 25 and 27, where in the latter work the $c(1 \times 3)\text{S}$ superstructure was formed by exposure to H_2S . The (3×1) sulphur superstructure described by Weissenrieder *et al.*²⁶ using thermal-induced segregation from bulk was not observed under our conditions.

The chemical purity of the $c(1 \times 3)\text{S}/\text{Fe}(110)$ superstructure was tested by Auger-electron spectroscopy. The Auger-intensity peak ratio was $\text{S}(152 \text{ eV})/\text{Fe}(651 \text{ eV})=0.24$ (for a primary electron energy of 3 keV) which is in accord with previous works.²⁵

B. Angular positions of FAD spots

In Fig. 4, we display two-dimensional intensity distributions (left column) as recorded with the microchannel plate detector for 0.6 keV and 0.8 keV ^3He atoms scattered from the $c(1 \times 3)\text{S}/\text{Fe}(110)$ and $c(2 \times 2)\text{O}/\text{Fe}(110)$ superstructures along $\langle 1\bar{1}\bar{1} \rangle$ (upper row), $\langle 001 \rangle$ (middle row), and $\langle 1\bar{1}\bar{0} \rangle$ (lower row) directions under polar incidence angles $0.6 \text{ deg} \leq \Phi_{\text{in}} \leq 1.2 \text{ deg}$. The projections of these intensity distributions are shown as functions of the azimuthal exit angle Ψ in the middle column. The number of diffraction spots as well as the azimuthal splittings $\Delta\Psi$ between adjacent peaks are different for both superstructures in each investigated channeling direction. For the scattering from $c(2 \times 2)\text{O}$ along $\langle 1\bar{1}\bar{1} \rangle$ and $\langle 001 \rangle$, the intensity maximum of the second diffraction order coincides with the maximum of the first order for $c(1 \times 3)\text{S}$ at the same azimuthal exit angle Ψ . In contrast, $\Delta\Psi$ along $\langle 1\bar{1}\bar{0} \rangle$ for $c(2 \times 2)\text{O}$ is larger than for $c(1 \times 3)\text{S}$ by a factor of 1.5, hence the peaks of the third order for $c(1 \times 3)\text{S}$ and the peaks of the second diffraction order for $c(2 \times 2)\text{O}$ coincide. These ratios are constant and independent of projectile species/isotopes and projectile energy.

In the right column of Fig. 4, we compare $\Delta\Psi$ as function of λ_{dB} for the scattering of H_2 molecules, ^3He and ^4He atoms for both superstructures. The slopes of the linear functions for $c(1 \times 3)\text{S}$ are twice as large as the slopes for $c(2 \times 2)\text{O}$ along $\langle 1\bar{1}\bar{1} \rangle$ and $\langle 001 \rangle$, but $2/3$ for $\langle 1\bar{1}\bar{0} \rangle$. For the small azimuthal exit angles Ψ investigated in our experiments, the linear dependence of the azimuthal angular splittings $\Delta\Psi$ of adjacent diffraction spots follows directly from the Bragg condition $n\lambda_{\text{dB}}=d \sin \Psi$ and is given by $\Delta\Psi \approx \lambda_{\text{dB}}/d$. Therefore, the slopes depend on the channel widths d only.

In Fig. 5, we compare for $c(1 \times 3)\text{S}$ (upper panel) and $c(2 \times 2)\text{O}$ (lower panel) the linear dependence of $\Delta\Psi$ on λ_{dB} for the four investigated channeling directions with different widths d . All data points shown in the right column of Fig. 4 and both panels of Fig. 5 represent the averaged azimuthal splitting of adjacent diffraction spots of different orders for a selected de Broglie wavelength λ_{dB} . The slopes s of

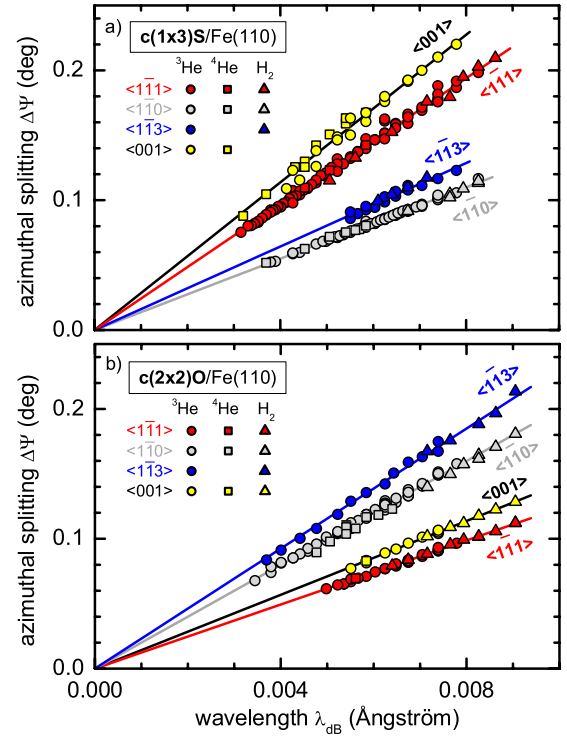


FIG. 5. (Color online) Azimuthal angular splitting $\Delta\Psi$ of diffraction spots as function of de Broglie wavelength λ_{dB} for scattering of H_2 molecules, ^3He and ^4He atoms from $c(1 \times 3)\text{S}/\text{Fe}(110)$ (upper panel) and $c(2 \times 2)\text{O}/\text{Fe}(110)$ (lower panel) along $\langle 1\bar{1}\bar{1} \rangle$ (red symbols), $\langle 1\bar{1}\bar{0} \rangle$ (gray symbols), $\langle 1\bar{1}\bar{3} \rangle$ (blue symbols), and $\langle 001 \rangle$ (yellow symbols) directions. Lines: best linear fits to data.

the linear fits and the resulting widths $d_{\text{exp}} \approx \lambda_{\text{dB}}/\Delta\Psi = 180 \text{ deg}/(s \cdot \pi)$ of axial channels are listed in Table I. For a comparison, we also list the widths d_{cal} calculated with the Fe lattice constant $g=2.86 \text{ \AA}$ (Ref. 24). The widths of the channels along $\langle 1\bar{1}\bar{1} \rangle$ and $\langle 001 \rangle$ for $c(1 \times 3)\text{S}$ are unchanged with respect to the Fe(110) face, whereas the widths along $\langle 1\bar{1}\bar{0} \rangle$ and $\langle 1\bar{1}\bar{3} \rangle$ are larger than for Fe(110) by a factor of 3. For the $c(2 \times 2)\text{O}$ superstructure, the widths of all four investigated axial channels are larger by a factor of 2 with respect to the Fe lattice (cf. Fig. 2). Within the accuracy for the experimentally deduced widths d_{exp} (limited to some percent owing to the uncertainties in projectile energy E_0 and the spatial detector calibration), their values accord well with the calculated widths d_{cal} for both superstructures, which result from multiplication of an integer with the theoretical widths for the Fe(110) substrate (cf. last column of Table I).

C. Intensity modulation of FAD spots

The second important feature of the diffraction patterns is the dependence of the relative intensities of diffraction spots on the projectile energy E_0 as well as on the polar incidence angle Φ_{in} . As an example, we show in Fig. 6 experimentally deduced projections of intensity distributions as function of the deflection angle Θ for the scattering of ^3He atoms with energies $0.45 \text{ keV} \leq E_0 \leq 1.4 \text{ keV}$ along $\langle 1\bar{1}\bar{0} \rangle$ under constant $\Phi_{\text{in}}=0.85 \text{ deg}$. In addition to the already discussed lin-

TABLE I. Slopes s of linear fits (cf. Fig. 5), channel widths d_{exp} deduced from slopes and d_{cal} calculated from structure models (cf. Fig. 2) for scattering from superstructures $c(1 \times 3)\text{S}/\text{Fe}(110)$ and $c(2 \times 2)\text{O}/\text{Fe}(110)$ along $\langle 1\bar{1}0 \rangle$, $\langle 1\bar{1}3 \rangle$, $\langle 1\bar{1}1 \rangle$, and $\langle 001 \rangle$ directions and ratios $d_{\text{exp}}/d_{\text{Fe}}$ calculated with channel widths for Fe(110) [lattice constant $g=2.86 \text{ \AA}$ (Ref. 23)].

	Direction	s (deg/ \AA)	d_{exp} (\AA)	d_{cal} (\AA)	$d_{\text{exp}}/d_{\text{Fe}}$
$c(1 \times 3)\text{S}/\text{Fe}(110)$	$\langle 1\bar{1}0 \rangle$	13.7 ± 0.4	4.2 ± 0.1	$3g/2=4.29$	2.9 ± 0.1
	$\langle 1\bar{1}3 \rangle$	16.1 ± 0.5	3.6 ± 0.1	$\sqrt{59}g/6=3.66$	2.9 ± 0.1
	$\langle 1\bar{1}1 \rangle$	24.2 ± 0.7	2.36 ± 0.07	$\sqrt{6}g/3=2.34$	1.01 ± 0.03
	$\langle 001 \rangle$	28.4 ± 0.8	2.02 ± 0.06	$g/\sqrt{2}=2.02$	1.00 ± 0.03
$c(2 \times 2)\text{O}/\text{Fe}(110)$	$\langle 1\bar{1}0 \rangle$	20.0 ± 0.6	2.9 ± 0.9	$g=2.86$	2.00 ± 0.06
	$\langle 1\bar{1}3 \rangle$	23.1 ± 0.7	2.5 ± 0.8	$\sqrt{59}g/9=2.44$	2.03 ± 0.06
	$\langle 1\bar{1}1 \rangle$	12.3 ± 0.4	4.6 ± 0.1	$2\sqrt{6}g/3=4.67$	1.99 ± 0.06
	$\langle 001 \rangle$	14.2 ± 0.4	4.0 ± 0.1	$\sqrt{2}g=4.05$	1.99 ± 0.06

ear relation between $\Delta\Psi$ and $\lambda_{\text{dB}}(E_0)$, Fig. 6 shows the change in the relative intensity of diffraction spots with E_0 . For example, for $E_0=0.45 \text{ keV}$ [cf. Fig. 6(a)] the intensity of the zeroth diffraction order is very weak, whereas the intensity for the first order is pronounced. At $E_0=0.75 \text{ keV}$ [Fig. 6(c)] the intensities for $n=0$ and 1 are almost equal, whereas the two peaks of the second order are larger by a factor of 2. This trend continues at an energy of $E_0=1 \text{ keV}$ [Fig. 6(e)],

where the intensity for $n=1$ vanishes and the intensity for the zeroth diffraction order is pronounced. The opposite changes in the intensities for $n=0$ and 1 are also present for scattering along $\langle 1\bar{1}3 \rangle$ as shown in Fig. 7.

These intensity variations are attributed to the corrugation of the interaction potential across the axial channels^{15,16} and can be understood within the semiclassical concept of *super-numerary rainbows*.⁴⁴ In addition to the interference of tra-

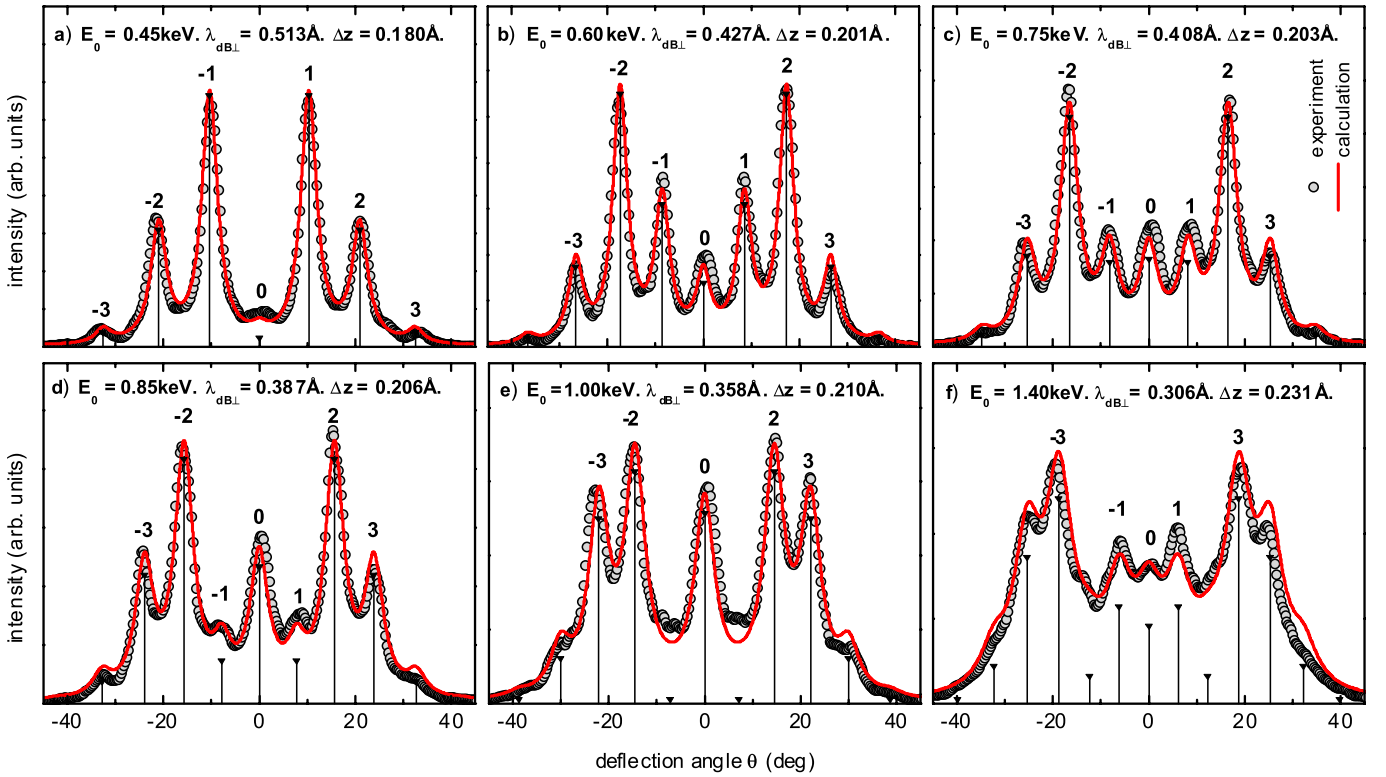


FIG. 6. (Color online) Gray circles: experimentally deduced projections of intensity distributions on deflection angle Θ for scattering of 0.45 keV (a), 0.60 keV (b), 0.75 keV (c), 0.85 keV (d), 1 keV (e), and 1.40 keV (f) ^3He atoms under polar incidence angle $\Phi_{\text{in}} = 0.85 \text{ deg}$ along $\langle 1\bar{1}0 \rangle$ from $c(2 \times 2)\text{O}/\text{Fe}(110)$. Red curves: superpositions of Lorentzian peaks. Black bars indicate angular positions and amplitudes of Lorentzian peaks which are deduced by Bragg conditions and square of Bessel functions $J_n(\Delta z, \lambda_{\text{dB}\perp})$, respectively, as detailed in text. Deduced full corrugation Δz is given in each panel. Diffraction orders n are labeled with numbers at intensity maxima.

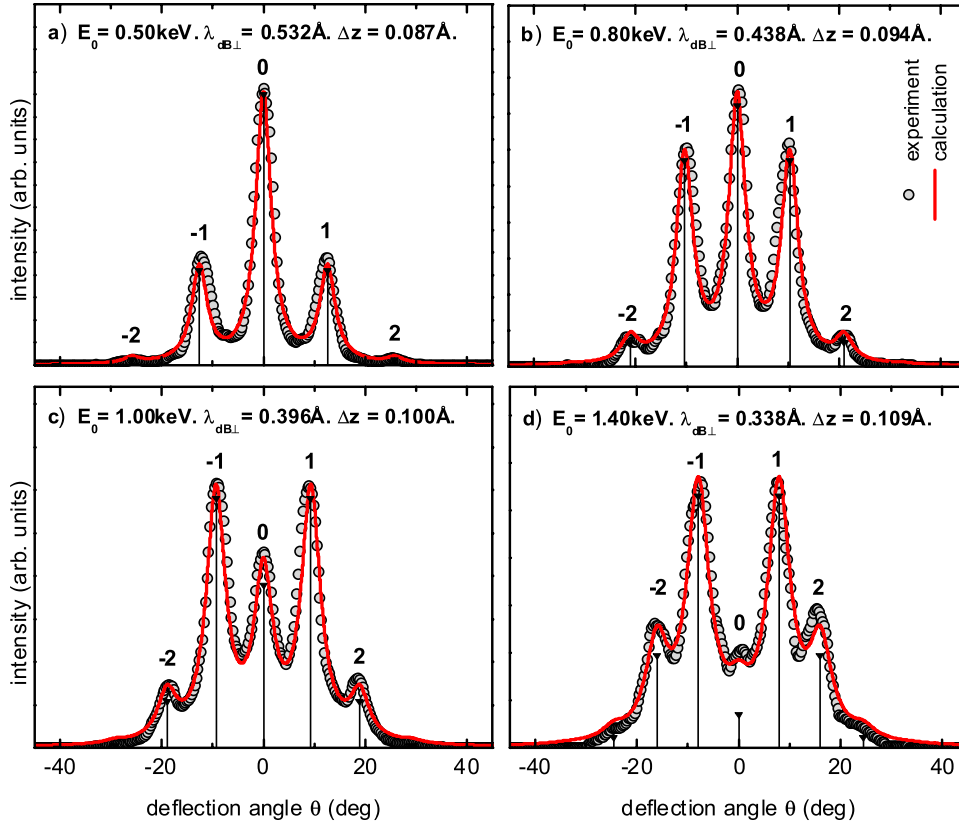


FIG. 7. (Color online) Same as in Fig. 6 for scattering of 0.5 keV (a), 0.8 keV (b), 1 keV (c), and 1.4 keV (d) ^3He atoms under $\Phi_{\text{in}} = 0.77$ deg along $\langle 1\bar{1}3 \rangle$ from $c(2 \times 2)\text{O}/\text{Fe}(110)$.

jectories deflected from equivalent sites of the equipotential faces separated by the widths d of axial channels, which is the origin for the appearance of diffraction spots (Bragg peaks), grazing scattering from a corrugated potential is affected by a second type of interference. Below the classical rainbow angle, for each deflection angle Θ a pair of trajectories deflected from different sites of the equipotential plane can be found. The phase difference between the two pathways determines the probability of scattering under a given angle Θ .^{16,44} This results in a characteristic intensity modulation of the diffraction spots of order n . The oscillations are similar to the atmospheric phenomenon⁴⁵ of supernumerary rainbows.^{44–47} From the analysis of the intensities of the diffraction spots, one can derive the corrugation of the interaction potential and information on the vertical positions of adsorbed atoms. We discuss this feature for the scattering of ^3He atoms from $c(2 \times 2)\text{O}/\text{Fe}(110)$ in Sec. III E.

In the semiclassical theory for scattering from a sinusoidal hard wall,^{46,48} the intensity I_n of a diffraction spot of order n is given by

$$I_n = J_n^2 \left(\frac{\pi \Delta z}{\lambda_{\text{dB}\perp}} [1 + \cos \Theta_n] \right), \quad (1)$$

with J_n being the Bessel function of order n , $\Theta_n = \arccos \sqrt{1 - (n\lambda_{\text{dB}\perp}/d)^2}$ the deflection angle of order n , and Δz the full corrugation of the sinusoidal hard wall, i.e., the normal distance between the maximum and the minimum of a equipotential surface. In Ref. 48 it was shown that this semiclassical approximation is in accord with the full quantum mechanical description^{48,49} in a wide range of $\lambda_{\text{dB}\perp}$. We

note that different “kinematic prefactors” can be found in literature.^{46,50–52} However, for our scattering geometry and for a small corrugation the prefactors can be neglected.⁸

In Fig. 8, we show the peak intensities for the diffraction orders $n=0$ (blue circles) and 1 (red squares) for scattering of ^3He atoms from $c(2 \times 2)\text{O}/\text{Fe}(110)$ along $\langle 1\bar{1}0 \rangle$ (panel a) and $\langle 1\bar{1}3 \rangle$ (panel c) as function of the normal de Broglie wavelength $\lambda_{\text{dB}\perp}$. The intensity for a specific diffraction order n is defined here as the area under the corresponding Lorentzian peak from a free fit of a superposition of Lorentzian peaks to all appearing diffraction spots of the experimentally deduced intensity distributions. In this manner, complete distributions are taken into account. The blue and red curves represent best correlated fits of intensities $I_n = J_n^2(2\pi\Delta z/\lambda_{\text{dB}\perp})$ for $n=0$ and 1, where $\cos \Theta_n \cong 1$. The full corrugation Δz of the He-surface interaction potential is assumed to depend on the normal energy as $\Delta z(E_{\perp}) = a \cdot E_{\perp} + b$, with a and b being fit parameters. This approach is different to the procedure in our recent paper,²⁰ where we evaluated the relative height of the zeroth and first-order diffraction spots with respect to the total intensity only. Since the full width at half maximum of the diffraction spots increase with increasing energy due to an enhanced decoherence ascribed to electronic excitations of the target surface,¹⁹ the oscillation amplitudes are damped. On the other hand, the contribution of the tails of adjacent diffraction spots increase due to the peak broadening and the decrease of the azimuthal splitting $\Delta\Psi$ between adjacent diffraction spots with increasing projectile energy E_0 . This results in an increasing offset of the intensity oscillations. We improved the fit procedure presented in Ref. 20 by taking into account an additional

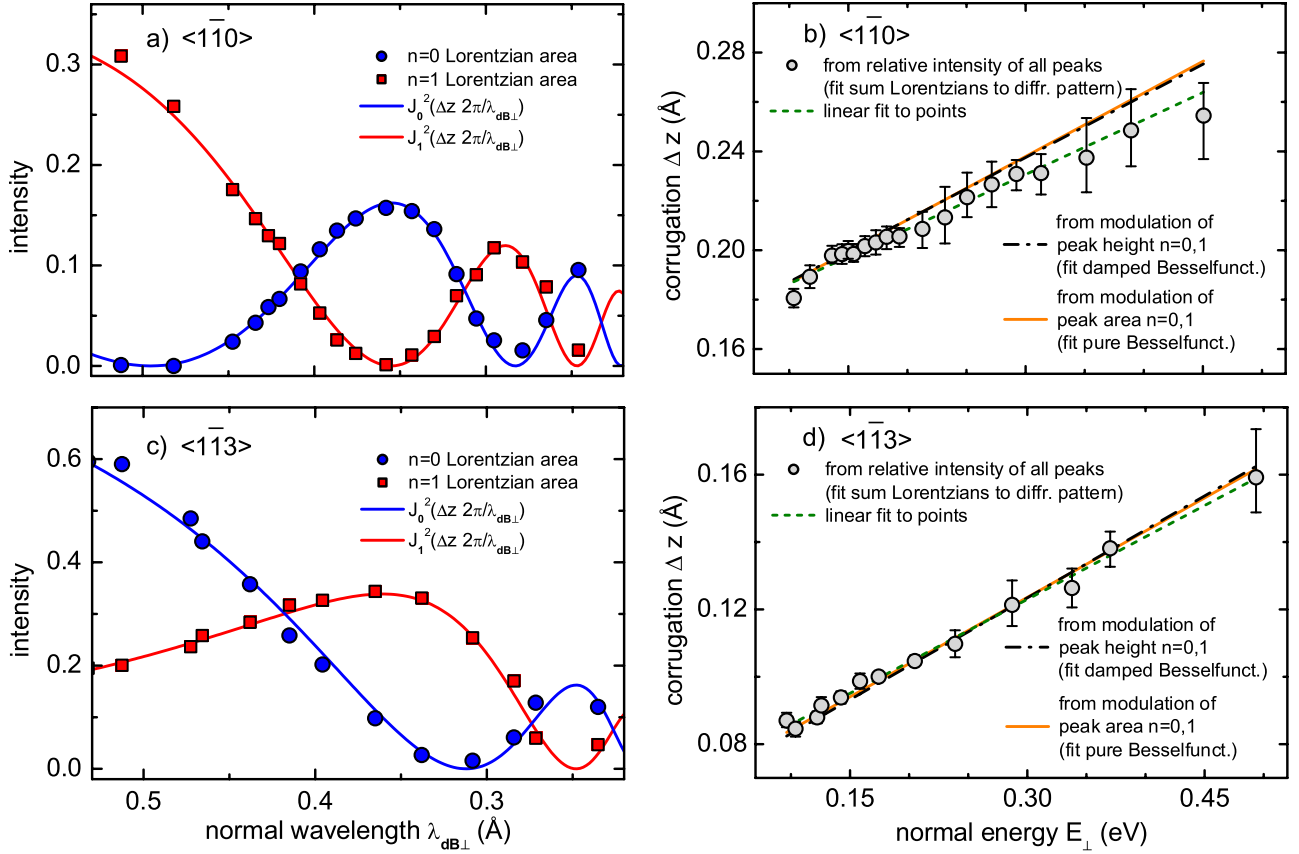


FIG. 8. (Color online) Left panels: Peak intensities for diffraction orders $n=0$ (blue circles) and 1 (red squares) defined as area of corresponding Lorentzian peaks from a free fit of a superpositions of Lorentzian peaks to all appearing diffraction spots of experimentally deduced projections of intensity distributions for scattering of ^3He atoms from $c(2 \times 2)\text{O}/\text{Fe}(110)$ along $\langle 1\bar{1}0 \rangle$ (a) and $\langle 1\bar{1}3 \rangle$ (c) directions (cf. Figs. 6 and 7). Blue and red curves represent best results from simultaneous fits of intensities $I_n = J_n^2(\Delta z 2\pi/\lambda_{dB\perp})$ for $n=0$ and 1, whereas full corrugation Δz is assumed to be linearly dependent on normal energy E_\perp (for details see text). Right panels: full corrugation Δz as function of E_\perp for scattering of ^3He atoms from $c(2 \times 2)\text{O}/\text{Fe}(110)$ along $\langle 1\bar{1}0 \rangle$ (b) and $\langle 1\bar{1}3 \rangle$ (d) directions. Red solid lines: linear function $\Delta z(E_\perp)$ resulting from best fits of (undamped) Bessel functions on intensity (Lorentzian area) modulation shown in left panels. Black dashed-dotted lines: linear functions $\Delta z(E_\perp)$ resulting from best fits of damped Bessel functions on modulation of diffraction peak amplitudes for $n=0$ and 1 from Ref. 20. Gray circles: results from best fits of relative intensities of all diffraction orders n for each diffraction pattern as detailed in text and shown as red curves in Figs. 6 and 7. Dashed lines: best linear fits to gray circles.

exponential damping term which hardly influences the position of the extrema and Δz . For comparison, the linear dependence of Δz on E_\perp from the fit with damped Bessel functions of the peak heights from Ref. 20 is plotted as black dashed-dotted lines in the right panels of Fig. 8. The fit parameters a and b are listed in Table II. The results are in good accord with those from the fit using undamped Bessel functions (solid lines).

A more accurate method to deduce the full corrugation is to take into account all diffraction spots. We fit a superposition of Lorentzian peaks to the normalized projected diffraction pattern, where the peak positions are given by the Bragg relation. We assume that the peak width is the same for all diffraction spots.¹⁹ The resulting relative peak heights are compared with the relative intensities given by Eq. (1) with Δz as fit parameter. Some calculated intensity distributions from the superposition of Lorentzian peaks are shown as red curves in Figs. 6 and 7. The amplitudes of the Lorentzian peaks are indicated by black bars and the values for Δz obtained from the fit are given in each panel of Figs. 6 and 7.

The deduced full corrugation Δz is plotted as function of the normal energy E_\perp in the right panels of Fig. 8 (gray circles).

TABLE II. Fit parameters a and b of relation $\Delta z = a \cdot E_\perp + b$ for assumed linear dependence of full corrugation Δz on normal energy E_\perp for different fit procedures of intensity modulations of diffraction spots using Bessel functions $J_n^2(\Delta z, \lambda_{dB\perp})$ for scattering of ^3He atoms from $c(2 \times 2)\text{O}/\text{Fe}(110)$ along $\langle 1\bar{1}0 \rangle$ and $\langle 1\bar{1}3 \rangle$ directions (upper row: parameters for red solid lines, middle row: black dashed-dotted lines and lower row: dotted lines as shown in right panels of Fig. 8).

Fit procedure	$\langle 1\bar{1}0 \rangle$		$\langle 1\bar{1}3 \rangle$	
	a (Å/eV)	b (Å)	a (Å/eV)	b (Å)
Undamped $J_{n=0,1}^2$	0.257	0.161	0.197	0.065
Damped $J_{n=0,1}^2$	0.252	0.162	0.202	0.063
All diffraction spots	0.221	0.164	0.186	0.067

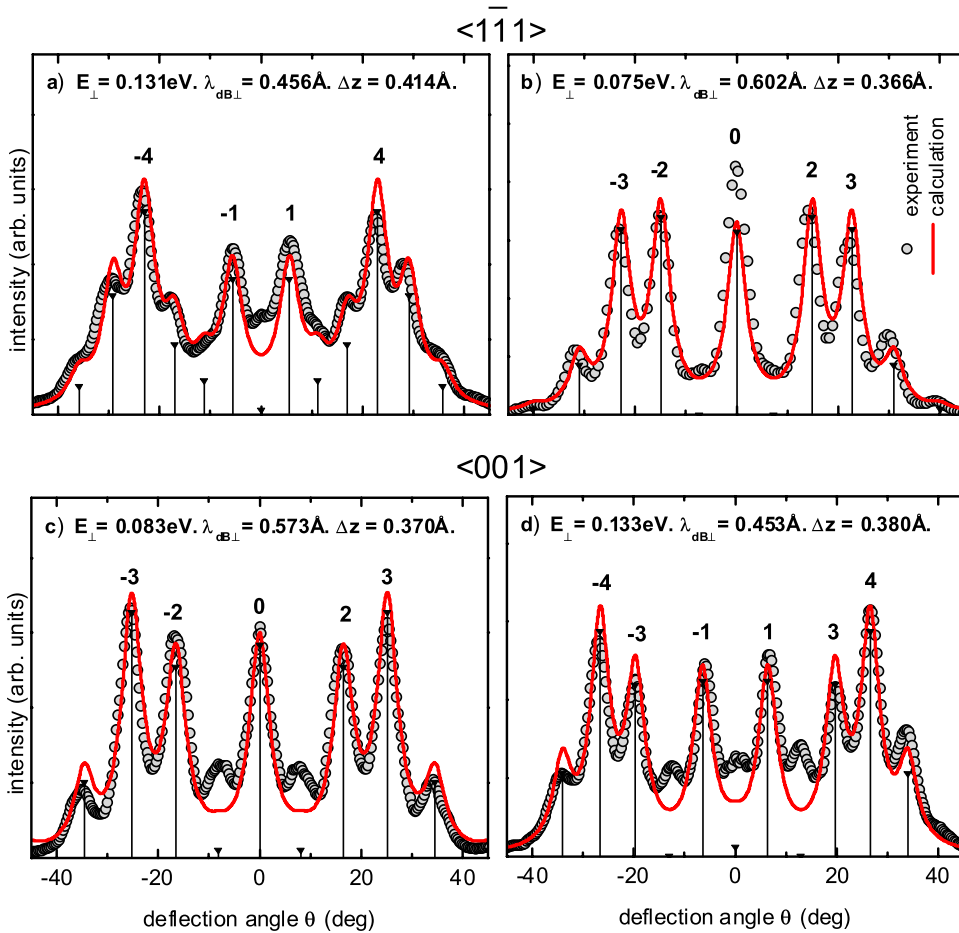


FIG. 9. (Color online) Same as in Fig. 6 for scattering of ${}^3\text{He}$ atoms with projectile energies $E_0 = 0.65$ keV under $\Phi_{\text{in}} = 0.81$ deg (a), $E_0 = 0.50$ keV under $\Phi_{\text{in}} = 0.70$ deg (b) along $\langle 1\bar{1}1 \rangle$, $E_0 = 0.5$ keV under $\Phi_{\text{in}} = 0.74$ deg (c), and 0.94 deg (d) along $\langle 001 \rangle$ from $c(2 \times 2)\text{O}/\text{Fe}(110)$.

Best linear fits $\Delta z(E_{\perp}) = a \cdot E_{\perp} + b$ to the data are given as dashed lines (parameters a and b are listed in Table II). For scattering along $\langle 1\bar{1}0 \rangle$ [Fig. 8(b)], the difference between these data and the results from the fits of Bessel functions J_0^2 and J_1^2 increases slightly with increasing normal energy E_{\perp} . This is caused by increased contributions of higher order ($n > 1$) diffractions spots to the total intensity of the diffraction pattern for larger E_{\perp} (cf. Fig. 6). However, for the scattering along $\langle 1\bar{1}3 \rangle$ [Fig. 8(d)] only the peaks of the second diffraction order contribute additionally at higher E_{\perp} (cf. Fig. 7). Thus, for $\langle 1\bar{1}3 \rangle$ we find good agreement between the three fit procedures.

We applied the same procedures to the projected intensity distributions measured for scattering of ${}^3\text{He}$ atoms from $c(2 \times 2)\text{O}/\text{Fe}(110)$ along the $\langle 1\bar{1}1 \rangle$ and $\langle 001 \rangle$ directions. The results are displayed in Fig. 9. In contrast to the projected intensity distributions shown in Figs. 6 and 7, the diffraction spots of higher orders ($n > 2$) appear already at lower-projectile energies $E_0 \approx 0.5$ keV. Furthermore, the angular splittings $\Delta\Psi$ between adjacent diffraction spots are smaller for $\langle 1\bar{1}1 \rangle$ and $\langle 001 \rangle$ than for $\langle 1\bar{1}0 \rangle$ and $\langle 1\bar{1}3 \rangle$. The linear dependencies of the full corrugation Δz on the normal energy E_{\perp} is deduced in a range of 0.07 eV $\leq E_{\perp} \leq 0.14$ eV. In this small normal energy range, Δz is fairly constant, and the intensity modulation of the different diffraction orders is determined by the changes in $\lambda_{\text{dB}\perp}$. In contrast, for scattering along $\langle 1\bar{1}0 \rangle$ and $\langle 1\bar{1}3 \rangle$ the intensity modulation of the differ-

ent diffraction orders depends on both $\lambda_{\text{dB}\perp}$ and $\Delta z(E_{\perp})$ (cf. right panels of Fig. 8).

In order to compare a complete data set consisting of a large number of individual projections of diffraction patterns as shown in Figs. 6, 7, and 9 with the calculation, we generate two-dimensional *diffraction charts*. In Fig. 10 we show the intensity of diffraction patterns as function of $\lambda_{\text{dB}\perp}$ and Θ as “three-dimensional” plots of experimental intensity distributions for the scattering of ${}^3\text{He}$ atoms from $c(2 \times 2)\text{O}/\text{Fe}(110)$ along $\langle 1\bar{1}0 \rangle$. This plot is generated from 21 projections of intensity distributions as shown in Fig. 6. For illustration, we have highlighted three projections from Figs. 6(b), 6(e), and 6(f) by black curves (cf. upper panel). For comparison between experiment and calculations, such two-dimensional diffraction charts contain rather complete information on the diffraction scenario. In Fig. 11, we display experimental (left panels) and calculated (right panels) diffraction charts for the scattering from $c(2 \times 2)\text{O}/\text{Fe}(110)$ along $\langle 1\bar{1}0 \rangle$ (upper panels) and $\langle 1\bar{1}3 \rangle$ (lower panels) directions. The two diffraction charts shown in the upper as well as in the lower panels, respectively, were generated using the same normalization and the same color code for the intensity. In addition to the intensity modulation of the diffraction spots, the plots in Fig. 11 show further important features: (1) While the angular position of the diffraction peaks of the different orders are determined by the periodicity of the interaction potential (Bragg condition indicated by dotted lines), the positions of the intensity maxima along these lines

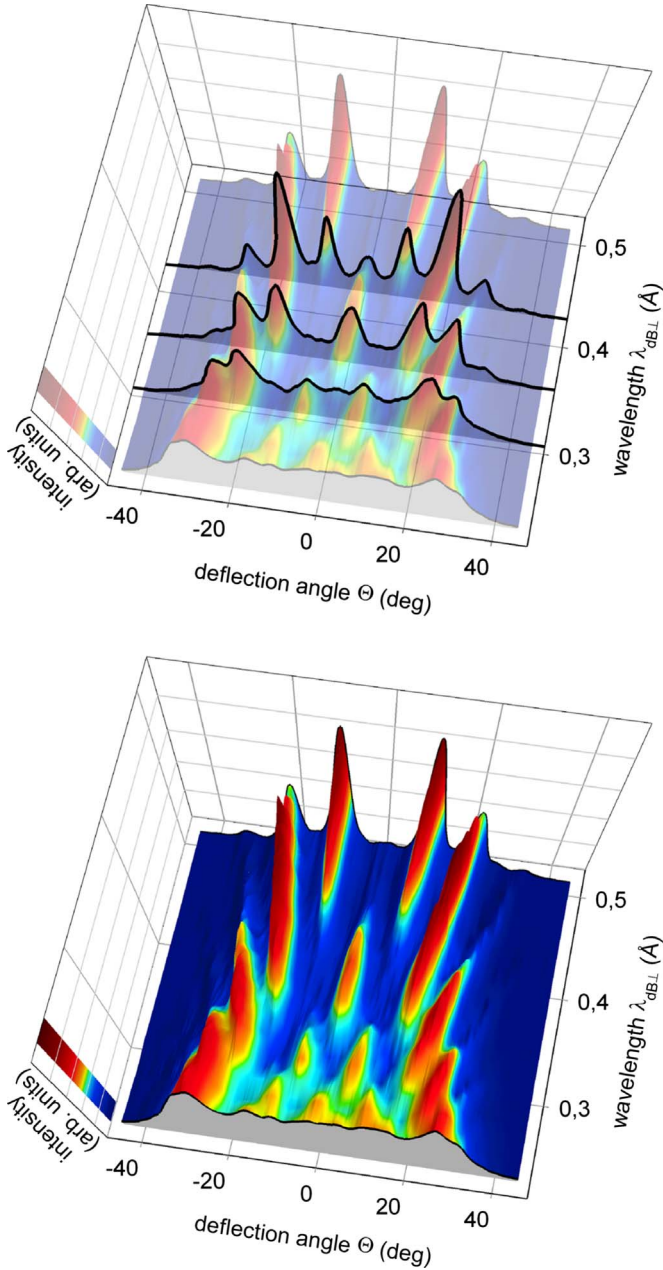


FIG. 10. (Color online) Three-dimensional plots of experimentally deduced intensities as function of deflection angle Θ and normal de Broglie wavelength $\lambda_{dB\perp}$ for scattering of ^3He atoms from $c(2\times 2)\text{O}/\text{Fe}(110)$ along $\langle 1\bar{1}0 \rangle$ (in upper and lower panel). The same data are shown as two-dimensional diffraction chart in Fig. 11(a). In upper panel, three projections of intensity distributions as shown in Figs. 6(b), 6(e), and 6(f) are highlighted as black curves. Color code: red=high intensity, blue=low intensity.

results from the full corrugation Δz of the interaction potential. Using the linear dependence $\Delta z(E_{\perp})=a \cdot E_{\perp}+b$ with the parameter a and b given in the lower line of Table II, we found good agreement between the experimental and calculated diffraction charts. (2) Furthermore, the transition from quantum diffraction to classical scattering can be identified in such diffraction charts: the diffraction patterns are increasingly blurred with decreasing de Broglie wavelength $\lambda_{dB\perp}$.

For $\lambda_{dB\perp} \lesssim 0.2 \text{ \AA}$, classical scattering dominates in terms of a relatively broad and diffuse angular distributions without diffraction spots. Then the classical rainbow peaks at the maxima of the deflection angle will remain.

D. Soft-potential correction

Beyond the hard-wall approximation, a more realistic semiclassical treatment should include the variation in the de Broglie wavelength along the trajectories due to the softness of the interaction potential. The comparison between hard- and soft-wall calculations shows that the hard-wall approximation mimics a reduced surface corrugation. Therefore, surface morphologies deduced in the framework of the hard-wall approximation are smoother than the real surface.⁴⁸ Hence, projectiles will be accelerated and decelerated differently depending on their impact parameter during the scattering process. This results in a phase difference for scattering from a soft potential and the hard wall. In order to evaluate this effect, we compare the calculated intensity modulation of the zeroth diffraction order for a soft potential with results for a hard wall with the same corrugation. The soft He-surface interaction potential is constructed “pairwise additive” as a sum over individual He-Fe and He-O pair potentials. The potential averaged along the axial channels (oriented in y direction) is obtained by superposition of axial string potentials between He projectiles and strings of Fe and O atoms of the topmost atomic layers resulting in a two-dimensional potential surface $V_s(x, z)$ (without corrugation in the direction of the strings of atoms). The axial string potential is given by^{21,22}

$$V_{\text{string}}(\rho) = \frac{1}{D} \int_{-\infty}^{\infty} V_{\text{ind}}(\sqrt{\rho^2 + y^2}) dy, \quad (2)$$

where ρ is the distance to the strings, D is the spacing between atoms of the strings of the axial channels, and V_{ind} is the interaction potential determined individually for He-Fe and for He-O. V_{ind} is calculated numerically in a statistical model taking into account electrostatic, kinetic, and exchange contributions.⁵⁵ The calculations are based on electron distributions for free atoms obtained from electron wave functions by Clementi and Roetti.⁵⁶ With these potentials we obtained good agreement with respect to the rainbow

TABLE III. Parameters α_i and β_i from fits of individual pair potentials He-Fe, He-O, and He-O(-) with Eq. (3).

Parameter	He-Fe	He-O	He-O(-)
α_1	-12.16291	-9.41497	-7.13300
α_2	-7.22431	-2.15148	-0.00935
α_4	4.07524	5.79838	1.41520
α_4	15.87682	7.88587	7.50770
β_1	0.81538	0.44297	0.38622
β_2	0.91849	0.63960	1.32971
β_3	0.71372	0.32351	0.63250
β_4	0.88033	0.55850	0.33911

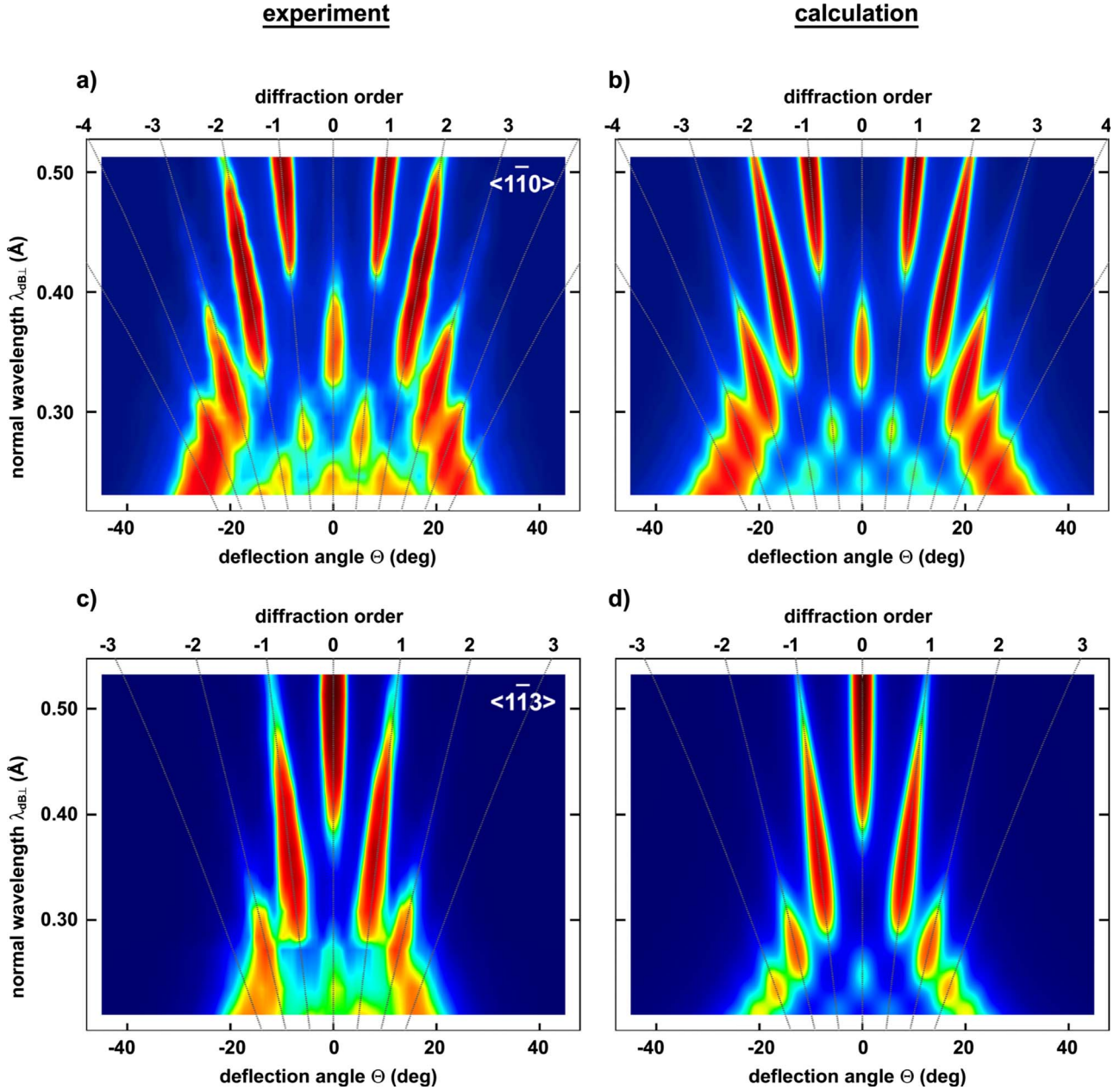


FIG. 11. (Color online) Experimentally deduced (left panels) and calculated (right panels) two-dimensional intensity distributions as function of deflection angle Θ and normal de Broglie wavelength $\lambda_{dB\perp}$ (diffraction charts) for scattering of ^3He atoms along $\langle 1\bar{1}0 \rangle$ (a and b) and $\langle 1\bar{1}3 \rangle$ (c and d) directions from $c(2 \times 2)\text{O}/\text{Fe}(110)$. Diffraction orders determined by Bragg condition $n\lambda_{dB\perp} = d \sin \Theta$ are indicated by dotted lines. Color code: red=high intensity, blue=low intensity.

angles^{57,58} for classical scattering at projectile energies of several keV^{59,60} (see Sec. III E). The calculated He-Fe and He-O interatomic potentials are plotted in Fig. 12. For potential energies below 50 eV, the individual pair potentials are well approximated by the analytical expression (in atomic units⁶¹)

$$V_{\text{ind}}(r) = \frac{Z_1 Z_2}{r} \sum_{i=1}^4 \alpha_i \exp(-r/\beta_i), \quad (3)$$

where r is the internuclear distance between two atomic partners with nuclear charges Z_1 and Z_2 . The parameters α_i and

β_i are given in Table III. The resulting potentials are plotted in Fig. 12 as red solid curves. Since our potential cannot correctly describe the He-surface van der Waals forces, we have neglected the attractive part of V_{ind} for the averaging using Eq. (2).

In Fig. 13, we display calculated equipotential planes $V_s(x, z) = \text{constant}$ (blue solid curves) for the scattering of He atoms from $c(2 \times 2)\text{O}/\text{Fe}(110)$ along $\langle 1\bar{1}0 \rangle$ (left panel) and $\langle 1\bar{1}1 \rangle$ (right panel) directions. The full corrugation Δz (marked for one equipotential plane) increases with increasing values of $V_s(x, z)$. Furthermore, Δz depends on the nor-

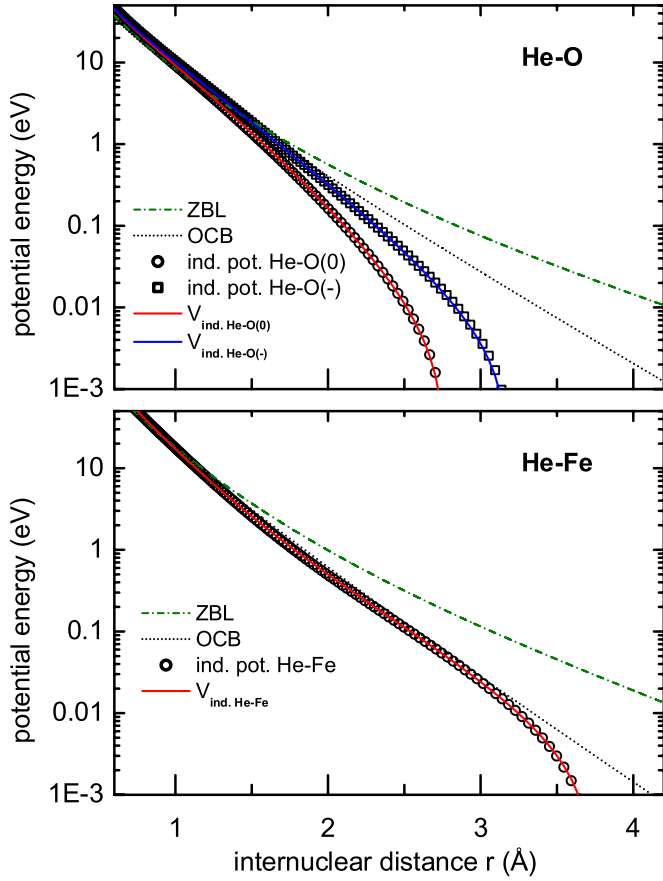


FIG. 12. (Color online) Interatomic potentials for He-O and He-O(-) (upper panel) and He-Fe (lower panel). Open circles: individual He-O and He-Fe potentials; open squares: individual He-O(-) potential (this work); solid red and blue curves through open circles and squares, respectively: analytical function $V_{\text{ind}}(r)$ for interpolation between calculated points (for details, see text); dashed-dotted green curves: ZBL potential (Ref. 53); dotted blue curves: OCB potential (Ref. 54).

mal distance h of the oxygen atoms at the Fe(110) surface (cf. Fig. 13). In order to justify the use of square of Bessel functions for the intensities I_n [cf. Eq. (1)] which are only valid for a purely sinusoidal corrugation, we display sinus functions (red dashed curves) in Fig. 13 in addition. For small normal energies $E_{\perp} \lesssim 2$ eV as relevant here, the corresponding equipotential lines are almost indistinguishable from a sinusoidal behavior. On such a corrugated potential, two different types of trajectories contribute to constructive interference. For the zeroth order diffraction spot (at $\Psi = \Theta = 0$ deg) these are (A) the scattering at the maximum above the strings of O atoms and (B) the scattering at the minimum of the potential between two adjacent strings of O atoms. From conservation of energy, the classical turning points of the trajectories coincide with $V_s(x, z) = E_{\perp}$ and their path difference is $2\Delta z$.

In order to calculate the interference for the two possible paths, we apply the semiclassical theory by Avrin and Merrill.⁴⁴ The phase difference $\Delta\phi$ is determined from two line integrals where the normal de Broglie wavelength $\lambda_{\text{dB}\perp}$ varies along the trajectories A and B:

$$\Delta\phi = 2\pi \left[\int_A \frac{dz}{\lambda_{\text{dB}\perp}^A(z)} - \int_B \frac{dz}{\lambda_{\text{dB}\perp}^B(z)} \right] - \frac{\pi}{2}. \quad (4)$$

The phase correction $-\pi/2$ reflects the phase change suffered by a wave as it passes through a focus.⁴⁴

In the hard-wall approximation, momentum as well as $\lambda_{\text{dB}\perp}$ are constant so that the phase difference is $\Delta\phi_{\text{hwa}} = 4\pi\Delta z/\lambda_{\text{dB}\perp} - \pi/2$. For the soft potential, one has to take into account the variation of $\lambda_{\text{dB}\perp}^{\text{A,B}}(z)$ along the entire classical trajectories. The phase difference $\Delta\phi_{\text{sp}}$ for the soft potential is calculated numerically on the basis of trajectory simulations using concepts of classical mechanics.

The normalized intensity $\hat{I}_0 = \frac{1}{4}|1 + \exp(i\Delta\phi)|^2 = \frac{1}{2}(1 + \cos\Delta\phi)$ (upper panel) and the phase difference $\Delta\phi$ (lower panel) calculated for the zeroth order diffraction spot are displayed in Fig. 14 as functions of the normal energy E_{\perp} for

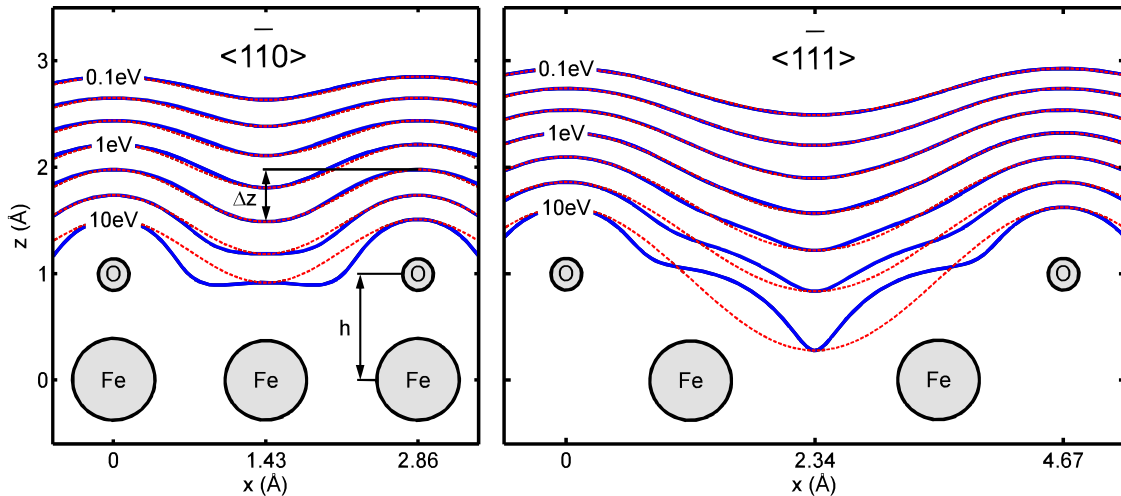


FIG. 13. (Color online) Sketch of arrangement of Fe and O atoms normal to $\langle 1\bar{1}0 \rangle$ (left panel) and $\langle 1\bar{1}\bar{1} \rangle$ (right panel) as well as equipotential lines $V_s(x, z) = \text{constant}$ in a range 0.1–10 eV for $c(2 \times 2)\text{O}/\text{Fe}(110)$. Blue solid curves: calculated equipotential planes; red dashed curves: sinus functions.

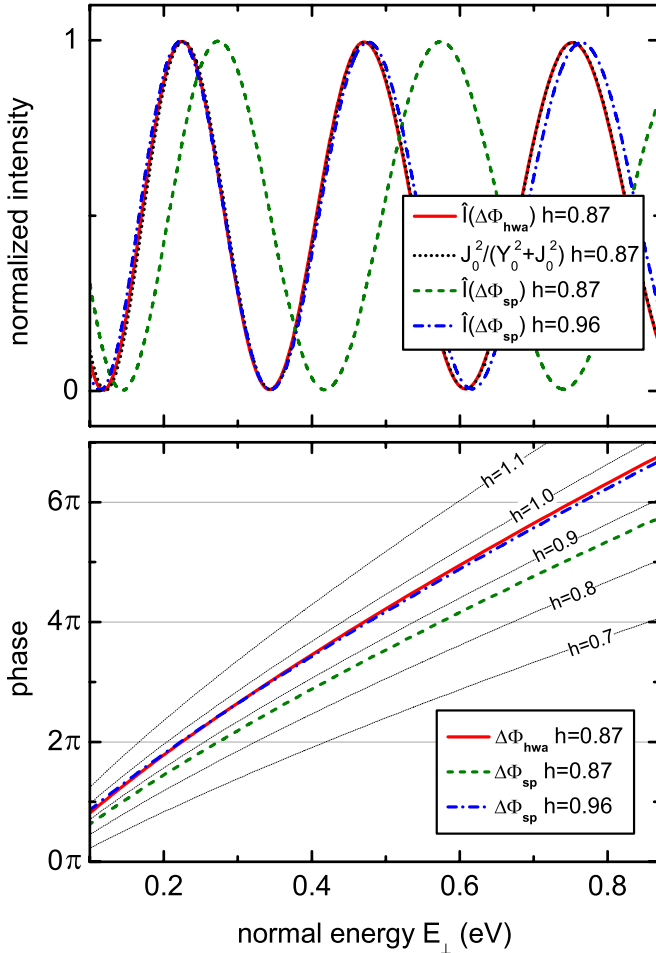


FIG. 14. (Color online) Normalized intensity $\frac{1}{4}|1+\exp(i\Delta\phi)|^2$ (upper panel) and phase difference $\Delta\phi$ (lower panel) calculated for zeroth order diffraction spot as functions of normal energy E_{\perp} for hard wall (solid red curves) and individual He-Fe/He-O potentials for normal distances $h=0.87$ Å (dashed green curves) and 0.96 Å (dashed-dotted blue curves) of oxygen atoms for scattering of ^3He atoms from $c(2\times 2)\text{O}/\text{Fe}(110)$ along $\langle 1\bar{1}0 \rangle$. Upper panel: dotted black curve: renormalized square of Bessel function for intensity $\hat{I}_0=J_0^2/(Y_0^2+J_0^2)$ (see text) calculated for $h=0.87$ Å. Lower panel: solid gray curves: phase difference as functions of normal energy for individual He-Fe/He-O potentials for different normal distances h .

the hard wall ($\Delta\phi_{\text{hwa}}$, red curves) and soft potential ($\Delta\phi_{\text{sp}}$, green curves) with $h=0.87$ Å, for the oxygen atoms of $c(2\times 2)\text{O}/\text{Fe}(110)$ and scattering of ^3He atoms along $\langle 1\bar{1}0 \rangle$. Furthermore, we show the intensity of the zeroth order diffraction spot calculated according to Eq. (1) for $h=0.87$ Å, as renormalized intensity $\hat{I}_0=J_0^2/(Y_0^2+J_0^2)$ (dotted black curve; Y_0 is the zeroth order Bessel function of second kind and $(Y_0^2+J_0^2)$ is the envelope function of J_0^2). The intensities \hat{I}_0 and \hat{I}_{hwa} for the hard-wall approximation almost coincide but the shift of the maxima of the intensity \hat{I}_{sp} for the soft potential is pronounced. This shift can be eliminated almost completely by an enhancement of Δz for the soft potential by increasing h to 0.96 Å (shown as blue curves in Fig. 14). In this manner one can correct Δz and h obtained for the hard-

wall approximation. This procedure was performed for the four investigated channeling directions as described in the next Sec. III E.

E. Vertical positions of adsorbed oxygen atoms

In order to relate the corrugation across the axial channels to the positions of O atoms at a distance h above the topmost Fe layer, we calculated Δz of the He-surface interaction potential $V_s(x, z)$ for different values of h . The He-surface interaction potential is constructed as described in Sec. III D by the superposition of axial-continuum potentials. In order to demonstrate the influence of the choice of interatomic interaction potential on the calculation of Δz and the resulting best fits for h , we also use pair potentials based on Thomas-Fermi screening with an adjusted screening length as proposed by O'Connor and Biersack⁵⁴ (OCB, dotted blue curves in Fig. 12). In recent studies,^{59,62} we have demonstrated that the OCB potential is more adequate for grazing scattering of fast atoms than the “universal potential” proposed by Ziegler, Biersack, and Littmark⁵³ (ZBL, dashed-dotted green curves in Fig. 12), which was found to be too repulsive at large internuclear distances r . ZBL as well as OCB are two prominent examples of generalized potentials, which provide analytic functions with respect to the internuclear distance r and the atomic numbers Z_1 and Z_2 . For many Z_1, Z_2 combinations, these potentials are good approximations, however, they do not take into account detailed electronic structures and features such as ionicity.⁶⁰

For adsorption of oxygen as covalently bound atoms with ionic character,^{23,32} one has to take into account that the interaction potential between a helium atom and an oxygen ion is different from the potential between a helium atom and an oxygen atom. We have calculated the individual potential for He atoms and O^- [indicated in the following as $\text{O}(-)$] ions (open squares in upper panel of Fig. 12). The fit with Eq. (3) is shown in Fig. 12 as blue curve and the fit parameters are listed in the last column of Table III. The individual He- $\text{O}(-)$ potential agrees well with a potential deduced from measurements of the mobility of $\text{O}(-)$ ions in He.⁶³

In Fig. 15, we show the calculated full corrugation Δz (gray curves) from individual He-Fe/He-O potentials for different h of the oxygen atoms for $c(2\times 2)\text{O}/\text{Fe}(110)$ along $\langle 1\bar{1}0 \rangle$ (panel a), $\langle 1\bar{1}1 \rangle$ (panel b), $\langle 1\bar{1}3 \rangle$ (panel c), and $\langle 001 \rangle$ (panel d). The full corrugations deduced from the experiments using the hard-wall approximation are represented by crosses. The best fit values for h based on the analysis using the OCB and individual He-Fe/He-O potentials are given in the second and third column of Table IV, respectively. For the $\langle 1\bar{1}0 \rangle$ and $\langle 1\bar{1}3 \rangle$ directions, the values for h deduced with the individual potentials are smaller than for the OCB potential used in our recent paper.²⁰ For $\langle 1\bar{1}1 \rangle$ and $\langle 001 \rangle$ this is reversed. In the following we consider the more appropriate individual potentials only.

Since h and Δz are different for soft potential and hard wall approximation, we apply the procedure described in Sec. III D to determine a corrected normal distance h^* and a correction of Δz , respectively. The corrected values for h^* for the individual He-Fe/He-O potentials are given in the fourth

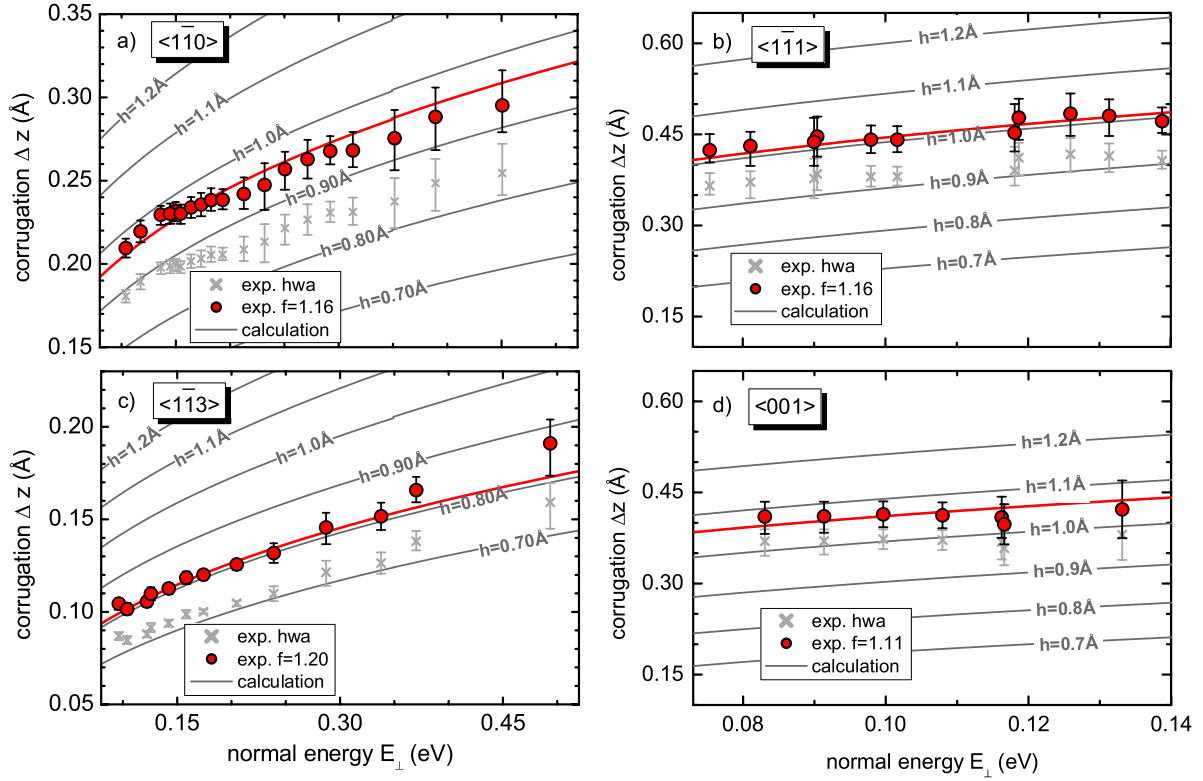


FIG. 15. (Color online) Full corrugation Δz as function of normal energy E_{\perp} for scattering of ${}^3\text{He}$ atoms from $c(2 \times 2)\text{O}/\text{Fe}(110)$ along $\langle 1\bar{1}0 \rangle$ (a), $\langle 1\bar{1}1 \rangle$ (b), $\langle 1\bar{1}3 \rangle$ (c), and $\langle 001 \rangle$ (d) directions. Crosses: best fits on the experimentally deduced projections of intensity distributions as shown in Figs. 6, 7, and 9 for all apparent peaks of different diffraction orders with hard-wall approximation. Red circles: correction of best fits (crosses) by multiplication with factor f (see text) deduced for individual He-Fe/He-O potentials. Solid curves: calculations with individual potentials for different h as indicated (gray curves) and h^* (red curves; cf. Table IV).

column of Table IV. The corrected Δz are shown as full red circles in Fig. 15. In a good approximation, the corrected Δz can be determined from the uncorrected values by scaling with a factor $f \approx \Delta z(h^*, E_{\perp}) / \Delta z(h, E_{\perp})$, which is given in the legends of Fig. 15. The full corrugations based on the corrected normal distances h^* are plotted as red curves. The scatter of h^* for the four axial channels is ascribed to deficiencies of the He-surface interaction potential, assuming free and undisturbed atoms and neglecting attractive contributions.

Taking into account the ionic nature of adsorbed oxygen, we calculated Δz from individual He-O(-) instead of neutral He-O potentials. The initial as well as the corrected values for h^* are listed in the fifth and sixth column of Table IV. For the He-Fe/He-O(-) potential, we obtain good agreement for

the rainbow angles Θ_{rb} for classical scattering^{59,60,62} at higher normal energies $E_{\perp} > 1$ eV for all investigated directions. As an example, we show in Fig. 16(c) the deflection angle Θ of the highest peak in the intensity distribution as function of E_{\perp} (red circles) for scattering of ${}^3\text{He}$ atoms from $c(2 \times 2)\text{O}/\text{Fe}(110)$ along $\langle 1\bar{1}0 \rangle$. For $E_{\perp} > 1$ eV, the highest peak corresponds to the classical rainbow peak as indicated in Fig. 16(b). However, for normal energies $E_{\perp} < 1$ eV, diffraction peaks appear as shown in Fig. 16(a), with discrete peaks that coincide with diffraction orders n as shown by the gray curves for $1 \leq n \leq 6$ in Fig. 16(c). The deflection angle of the intensity maximum named *quantum surface rainbow* is slightly smaller than the corresponding classical rainbow angle.⁴⁶ On the other hand, diffraction peaks in the classically forbidden “dark” region of the rainbow are present. The

TABLE IV. Normal distances for O atoms at fourfold hollow sites of Fe lattice in Å calculated for OCB (Ref. 54) and individual He-Fe/He-O and He-Fe/He-O(-) potentials. $h_{\text{He-O}}$ and $h_{\text{He-O(-)}}$: deduced using hard-wall approximation; $h_{\text{He-O}}^*$ and $h_{\text{He-O(-)} }^*$: including soft potential correction.

Direction	h_{OCB}	$h_{\text{He-O}}$	$h_{\text{He-O}}^*$	$h_{\text{He-O(-)}}$	$h_{\text{He-O(-)} }^*$
$\langle 1\bar{1}0 \rangle$	1.15	0.87	0.96	0.87	0.95
$\langle 1\bar{1}3 \rangle$	1.06	0.72	0.81	0.75	0.85
$\langle 1\bar{1}1 \rangle$	0.70	0.93	1.01	0.75	0.80
$\langle 001 \rangle$	0.91	1.0	1.06	0.85	0.88

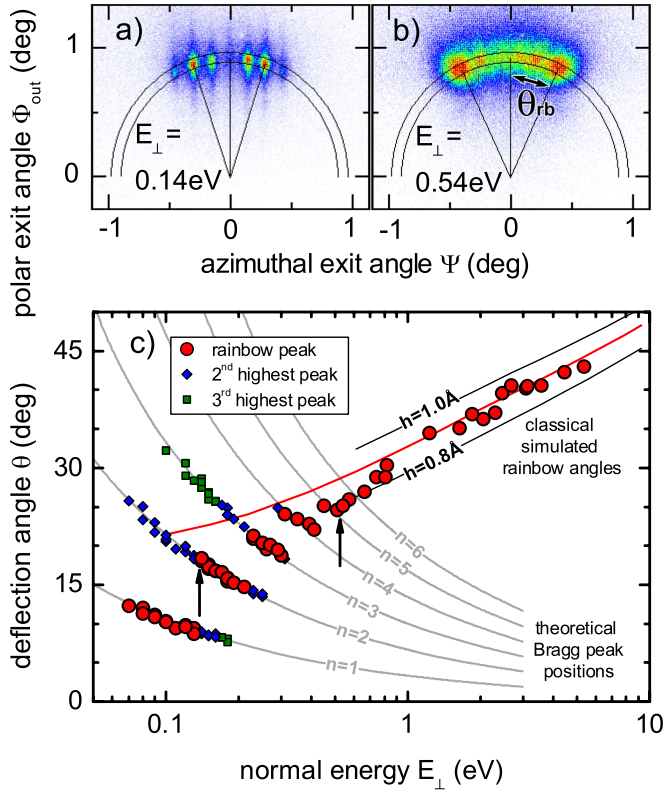


FIG. 16. (Color online) Upper panels: two-dimensional intensity distributions for scattering of 0.5 keV (a) and 2.0 keV (b) ^3He atoms along $\langle 1\bar{1}0 \rangle$ from $c(2 \times 2)\text{O}/\text{Fe}(110)$ under $\Phi_{\text{in}} = 0.94$ deg. Color code: red=high intensity, blue=low intensity. Lower panel: Deflection angle θ as function of normal energy E_{\perp} for diffraction orders $1 \leq n \leq 6$. Gray curves determined by Bragg condition. Red circles: angular position of highest peaks (rainbow peaks), blue diamonds: second highest peaks and green squares: third highest peaks in diffraction patterns. Black arrows indicate values deduced from intensity distributions shown in panels a and b. For higher normal energies $E_{\perp} > 1$ eV, red circles represent classical rainbow angle Θ_{rb} as indicated in panel b. Red and black curves: dependence of Θ_{rb} on E_{\perp} resulting from simulations using individual potentials (cf. Fig. 12) for different normal distances h (thick solid red curve $h=0.9$ Å) of O atoms above Fe lattice.

deflection angle of the second and the third highest diffraction peaks are displayed as blue diamonds and green squares, respectively. The data points from the intensity distributions shown in Figs. 16(a) and 16(b) are highlighted by black arrows in Fig. 16(c). The plot illustrates the transition from quantum diffraction to classical scattering at higher energies. Results from classical trajectory calculations using different values for h of the oxygen atoms are shown as solid red and black curves in Fig. 16(c). For $h=0.9$ Å (thick solid red curve), the calculated dependence of the classical rainbow angle Θ_{rb} on E_{\perp} agrees with the experiments. This value for h is in accord with $h^*=0.95$ Å, as deduced from evaluation of the diffraction patterns using individual He-Fe/He-O(-) potentials. This holds for all four investigated axial channels (not shown) which demonstrates the consistency of our present analysis.

The scatter of h^* for the four investigated channeling directions (cf. Table IV) is significantly larger than the accuracy of our analysis of the FAD data. For a perfect description of the potential, h^* should be independent of the channeling direction. FAD has a high-intrinsic precision but the accuracy of h^* is presently limited by uncertainties of the He-surface interaction potential. Hence, our current result of $h^*=(0.9 \pm 0.2)$ Å could be improved in accuracy by having a more sophisticated interaction potential available. We note that our value for h^* is in accord with DFT calculations. For an oxygen coverage of $\theta=1/4$ ML on Fe(110) [which corresponds to the $c(2 \times 2)\text{O}/\text{Fe}(110)$ superstructure] $h=1.0$ Å was reported in Ref. 39. For a coverage between 0.22 and 0.44 ML, h amounts between 1.07 Å and 1.11 Å, respectively.⁴² These results agree with findings from Erley and Ibach,³⁰ where an assumed bonding length of 1.8 Å, between the Fe and O atoms accords with the stretching frequency observed for free FeO molecules by vibrational electron-energy-loss spectroscopy (EELS). For fourfold hollow sites of the adsorbed oxygen atoms this bonding length corresponds to $h=1.1$ Å.

IV. CONCLUSIONS

We have observed diffraction patterns for axial surface channeling of fast neutral H_2 molecules, ^3He and ^4He atoms along the $\langle 1\bar{1}0 \rangle$, $\langle 1\bar{1}3 \rangle$, $\langle 1\bar{1}1 \rangle$, and $\langle 001 \rangle$ directions from a Fe(110) surface covered by $c(2 \times 2)$ and $c(1 \times 3)$ superstructures formed by the adsorption of O and S atoms, respectively. From the azimuthal angular splittings of diffraction spots, we deduce the widths of the axial channels and find good agreement with values from the substrate crystal lattice. From intensity modulations of diffraction spots we derive the full corrugation Δz as well as the normal distance h of oxygen atoms above the Fe lattice for the $c(2 \times 2)\text{O}/\text{Fe}(110)$ superstructure. The analysis is based on detailed two-dimensional diffraction charts.

The experimental Δz are compared with calculated values for different h using the hard-wall approximation and individual He-Fe/He-O soft-interaction potentials. The calculations were performed for adsorbed neutral oxygen atoms and oxygen ions using modified individual potentials He-O and He-O⁻, respectively. Since for the same h , the full corrugation Δz differs for the hard-wall approximation and the soft-interaction potential, we introduced a corrected normal distance h^* and a corrected full corrugation for our results obtained in the framework of the hard-wall approximation. Our final value $h^*=(0.9 \pm 0.2)$ Å is in accord with DFT calculations and corresponds to the bonding length of Fe and O atoms estimated from EELS experiments. We point out that the determination of the full corrugation using FAD has a high-intrinsic precision, but the accuracy is limited by uncertainties in the knowledge on the interaction potential. This work demonstrates that fast atom diffraction is a powerful method for the analysis of surface structures, which combines benefits of techniques related to real space and diffraction. FAD is virtually nondestructive due to the grazing scattering of light atoms and molecules with fluxes of about 10^3 incident particles per second, has high detection efficiency,

and can be applied at room or higher temperatures without charging effects. Hence, this method is even applicable in investigations on sensitive surface structures, where established techniques as LEED, RHEED, TEAS, or HAS might fail.

ACKNOWLEDGMENTS

We thank the DFG (Project No. Wi 1336) for financial support and K. Maass, H. Grundmann, G. Lindenberg, and U. Linke (FZ Jülich) for their assistance in the preparation and running of the experiments.

*Author to whom correspondence should be addressed; mbusch@physik.hu-berlin.de

- ¹L. de Broglie, *Nature* (London) **112**, 527 (1923).
- ²C. Davisson and L. H. Germer, *Phys. Rev.* **30**, 705 (1927).
- ³I. Estermann and A. Stern, *Z. Phys.* **61**, 95 (1930).
- ⁴M. A. Van Hove, W. Moritz, H. Over, P. J. Rous, A. Wander, A. Barbieri, N. Materer, U. Starke, and G. A. Somorjai, *Surf. Sci. Rep.* **19**, 191 (1993).
- ⁵K. Heinz, *Prog. Surf. Sci.* **27**, 239 (1988).
- ⁶J. E. Mahan, K. M. Geib, G. Y. Robinson, and R. G. Long, *J. Vac. Sci. Technol. A* **8**, 3692 (1990).
- ⁷D. Farias and K.-H. Rieder, *Rep. Prog. Phys.* **61**, 1575 (1998).
- ⁸*Helium Atom Scattering from Surfaces*, edited by E. Hulpke (Springer-Verlag, Berlin, 1982).
- ⁹J. P. Toennies, *Appl. Phys. (Berlin)* **3**, 91 (1974).
- ¹⁰R. D. Ramsier and J. T. Yates, *Surf. Sci. Rep.* **12**, 246 (1991).
- ¹¹H. Tokutaka, M. Prutton, I. G. Higginbotham, and T. E. Gallon, *Surf. Sci.* **21**, 233 (1970).
- ¹²J. Harnett, S. Haq, and A. Hodgson, *Surf. Sci.* **528**, 15 (2003).
- ¹³J. P. Toennies, F. Traeger, J. Vogt, and H. Weiss, *J. Chem. Phys.* **120**, 11347 (2004).
- ¹⁴A. Schüller, S. Wethekam, and H. Winter, *Phys. Rev. Lett.* **98**, 016103 (2007).
- ¹⁵P. Rousseau, H. Khemliche, A. G. Borisov, and P. Roncin, *Phys. Rev. Lett.* **98**, 016104 (2007).
- ¹⁶A. Schüller and H. Winter, *Phys. Rev. Lett.* **100**, 097602 (2008).
- ¹⁷A. Schüller and H. Winter, *Nucl. Instrum. Methods Phys. Res. B* **267**, 628 (2009).
- ¹⁸N. Bundaleski, H. Khemliche, P. Soullise, and P. Roncin, *Phys. Rev. Lett.* **101**, 177601 (2008).
- ¹⁹M. Busch, A. Schüller, S. Wethekam, and H. Winter, *Surf. Sci.* **603**, L23 (2009).
- ²⁰A. Schüller, M. Busch, S. Wethekam, and H. Winter, *Phys. Rev. Lett.* **102**, 017602 (2009).
- ²¹D. Gemmell, *Rev. Mod. Phys.* **46**, 129 (1974).
- ²²H. Winter, *Phys. Rep.* **367**, 387 (2002).
- ²³C. Leygraf and S. Ekelund, *Surf. Sci.* **40**, 609 (1973).
- ²⁴G. Gafner and R. Feder, *Surf. Sci.* **57**, 37 (1976).
- ²⁵S. R. Kelemen and A. Kaldor, *J. Chem. Phys.* **75**, 1530 (1981).
- ²⁶J. Weissenrieder, M. Göthelid, G. Le Lay, and U. O. Karlsson, *Surf. Sci.* **515**, 135 (2002).
- ²⁷L. Berbil-Bautista, S. Krause, T. Hänke, M. Bode, and R. Wiesendanger, *Surf. Sci.* **600**, L20 (2006).
- ²⁸A. J. Pignocco and G. E. Pellissier, *Surf. Sci.* **7**, 261 (1967).
- ²⁹A. J. Melmed and J. J. Carroll, *J. Vac. Sci. Technol.* **10**, 164 (1973).
- ³⁰W. Erley and H. Ibach, *Solid State Commun.* **37**, 937 (1981).
- ³¹Y. Sakisaka, T. Komeda, T. Miyano, M. Onchi, S. Masuda, Y. Harada, K. Yagi, and H. Kato, *Surf. Sci.* **164**, 220 (1985).
- ³²T. Miyano, Y. Sakisaka, T. Komeda, and M. Onchi, *Surf. Sci.* **169**, 197 (1986).
- ³³A. Wight, N. G. Condon, F. M. Leibsle, G. Worthy, and A. Hodgson, *Surf. Sci.* **331-333**, 133 (1995).
- ³⁴H.-J. Kim and E. Vescovo, *Phys. Rev. B* **58**, 14047 (1998).
- ³⁵M. Busch, M. Gruyters, and H. Winter, *Surf. Sci.* **600**, 4598 (2006).
- ³⁶M. J. S. Spencer, A. Hung, I. K. Snook, and I. Yarovsky, *Surf. Sci.* **540**, 420 (2003).
- ³⁷M. J. S. Spencer, I. K. Snook, and I. Yarovsky, *J. Phys. Chem. B* **109**, 9604 (2005).
- ³⁸M. J. S. Spencer, I. K. Snook, and I. Yarovsky, *J. Phys. Chem. B* **110**, 956 (2006).
- ³⁹P. Błoński, A. Kiejna, and J. Hafner, *Surf. Sci.* **590**, 88 (2005).
- ⁴⁰P. Błoński, A. Kiejna, and J. Hafner, *J. Phys.: Condens. Matter* **19**, 096011 (2007).
- ⁴¹P. Błoński and A. Kiejna, *Surf. Sci.* **601**, 123 (2007).
- ⁴²P. Błoński, A. Kiejna, and J. Hafner, *Phys. Rev. B* **77**, 155424 (2008).
- ⁴³Roentdek GmbH, Kelkheim-Ruppertsheim, Germany.
- ⁴⁴W. F. Avrin and R. P. Merrill, *Surf. Sci.* **311**, 269 (1994).
- ⁴⁵R. L. Lee, *J. Appl. Opt.* **37**, 1506 (1998).
- ⁴⁶U. Garibaldi, A. C. Levi, R. Spadacini, and G. E. Tommei, *Surf. Sci.* **48**, 649 (1975).
- ⁴⁷G. Boato, P. Cantini, U. Garibaldi, A. C. Levi, L. Mattera, R. Spadacini, and G. E. Tommei, *J. Phys. C* **6**, L394 (1973).
- ⁴⁸R. I. Masel and R. P. Merrill, *J. Chem. Phys.* **65**, 2690 (1976).
- ⁴⁹R. I. Masel, R. P. Merrill, and W. H. Miller, *Phys. Rev. B* **12**, 5545 (1975).
- ⁵⁰G. Boato, P. Cantini, and L. Mattera, *Surf. Sci.* **55**, 141 (1976).
- ⁵¹C. Chioldi and A. C. Levi, *Surf. Sci.* **59**, 325 (1976).
- ⁵²N. R. Hill and V. Celli, *Surf. Sci.* **75**, 577 (1978).
- ⁵³J. F. Ziegler, J. P. Biersack, and U. Littmark, *The Stopping and Range of Ions in Solids* (Pergamon, New York, 1985), Vol. I.
- ⁵⁴D. J. O'Connor and J. Biersack, *Nucl. Instrum. Methods Phys. Res. B* **15**, 14 (1986).
- ⁵⁵K. Gärtner and K. Hehl, *Phys. Status Solidi B* **94**, 231 (1979).
- ⁵⁶E. Clementi and C. Roetti, *At. Data Nucl. Data Tables* **14**, 177 (1974).
- ⁵⁷A. W. Kleyn and T. C. M. Horn, *Phys. Rep.* **199**, 191 (1991).
- ⁵⁸A. Schüller, G. Adamov, S. Wethekam, K. Maass, A. Mertens, and H. Winter, *Phys. Rev. A* **69**, 050901(R) (2004).
- ⁵⁹A. Schüller, S. Wethekam, A. Mertens, K. Maass, H. Winter, and K. Gärtner, *Nucl. Instrum. Methods Phys. Res. B* **230**, 172 (2005).
- ⁶⁰A. Schüller, K. Gärtner, and H. Winter, *Europhys. Lett.* **81**, 37007 (2008).
- ⁶¹Atomic units are used: energy: 1 a.u.=27.21 eV, length: 1 a.u.=0.529 Å.
- ⁶²A. Schüller and H. Winter, *Nucl. Instrum. Methods Phys. Res. B* **261**, 578 (2007).
- ⁶³A. A. Viggiano, R. A. Morris, and E. A. Mason, *J. Chem. Phys.* **98**, 6483 (1993).